

Taylor dispersion in arbitrarily shaped axisymmetric channels

Ray Chang[†] and Juan G. Santiago^{*,‡}

[†]*Department of Bioengineering, Stanford University, Stanford, CA, 94305, United States*

[‡]*Department of Mechanical Engineering, Stanford University, Stanford, CA, 94305, United States*

E-mail: juan.santiago@stanford.edu

Abstract

Advective dispersion of solutes in long thin axisymmetric channels is important to the analysis and design of a wide range of devices, including chemical separations systems and microfluidic chips. Despite extensive analysis of Taylor dispersion in various scenarios, all previous analyses have not been able to provide a simple prediction of the long-term spatial evolution of solute for arbitrary Pe_a . In the current study, we analyze the Taylor-Aris dispersion for arbitrarily shaped axisymmetric channels. We derive an expression for solute dynamics in terms of two coupled, closed-form ordinary differential equations (ODEs). These two ODEs allow prediction of the time evolution of the solute zone based on channel geometry alone. We compare and benchmark our predictions with Brownian dynamics simulations for a variety of cases including linearly expanding/converging and periodic channels. We also present a closed-form analytical description of the physical regimes of positive versus negative variance growth. Finally, to further demonstrate the utility of the analysis, we demonstrate a method to simply engineer channel geometries to achieve desired variance distribution. We apply the latter analysis to generate a geometry that results in a constant variance and a second geometry that results in a sinusoidal variance in space.

1 Introduction

Advective dispersion of solutes in long thin tubes is important to the design and optimization of a wide range of devices, from chemical processing and separations systems to microfluidic chips.¹ G. I. Taylor first reported a closed form solution for the long-term dispersive behavior of a solute in a circular cylindrical tube driven by a Poiseuille flow.² Taylor's original solution considered a regime where axial diffusion is negligible and is applicable for $L/a \gg Pe_a \gg 6.9$, where L is the characteristic channel length, a is the radius of the tube, and Pe_a is a Peclet number based on radius, a . Aris later included the effects of axial diffusion of the solute and introduced the method of moments which enabled treatment of all stages of the dispersive process in long-thin channels with fairly arbitrary cross-sections.³ Dispersion analyses including axial diffusion and

dynamic regimes where radial diffusion times are much shorter than advection times are typically termed Taylor-Aris analyses. Since these seminal papers, there have been much work analyzing the dispersion behavior in various systems. The book of Brenner & Edwards includes a broad range example analyses including effects of porous media, chemical reactions, and surface adsorption.¹ One notable analytical derivation is that of Bryden & Brenner, who analyzed the Taylor-Aris dispersion in diverging conical channel and a flared, axisymmetric Venturi tube geometry.⁴ They used multiple-timescale analysis to obtain an asymptotic expression for the effective dispersion coefficient and derived a partial differential equation (PDE) for a conditional probability density function describing the solute. However, the latter work neither provided a solution for this PDE nor analyzed the long-term dispersion and growth of a solute zone.

Another analytical study relevant to the current work is that of Hoagland & Prud'Homme,⁵ who analyzed Taylor-Aris dispersion in a long-thin, axisymmetric channel with a sinusoidal variation of radius along the streamwise direction using the method of moments. They presented numerical solutions of the method of moments for arbitrary wavelengths. They also derived an analytical expression for the long-term dispersion of solute in the limit of long wavelength which compared well with their numerical model. Adrover et al⁶ later considered dispersion of both point- and finite-sized particles in a long-thin sinusoidal channel. For point-size particles, they obtained various asymptotic expressions for the effective, long-term dispersion coefficient in the limits of large and small Pe_a . To our knowledge, all previous analyses were not able to provide a simple prediction of the long-term spatial evolution of solute for arbitrary Pe_a . We also know of no analytical work toward Taylor-Aris dispersion in an arbitrarily-shaped axisymmetric channel. Such analyses have significant potential to influence the design and analyses of a wide range of systems, including microfluidic devices. In the current study, we analyze the Taylor-Aris dispersion in an arbitrarily-shaped axisymmetric channel. We derive an expression for solute dynamics in terms of two coupled, closed-form ordinary differential equations (ODEs). These two ODEs enable prediction of the time evolution of the solute zone based on channel geometry alone. We compare and benchmark our predictions with Brownian dynamics simulations for a variety of cases. We

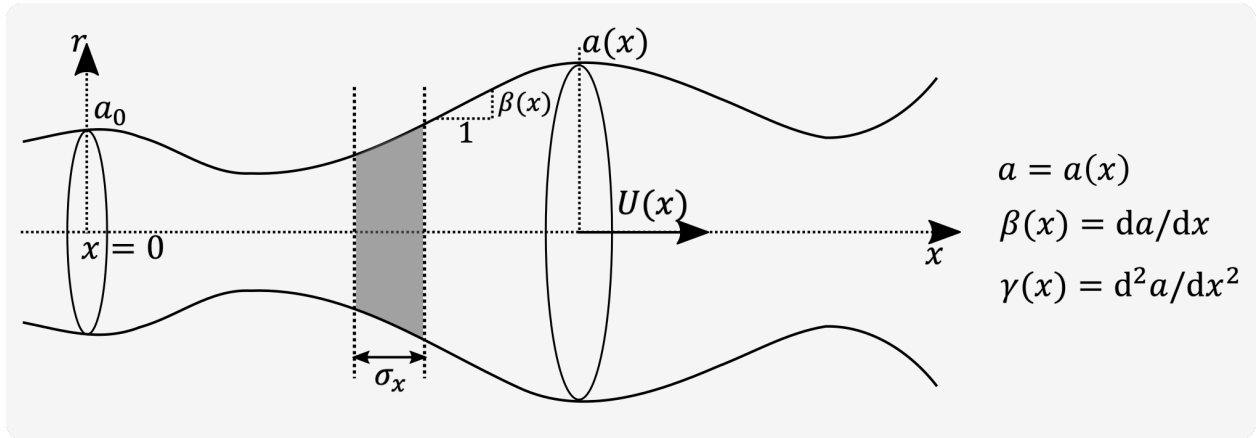


Figure 1: Schematic of an axisymmetric channel with a slowly varying, arbitrary distribution of radius, $a(x)$. A nominal radius is taken as a_0 at $x = 0$. The slope and the curvature of the cylinder wall are respectively $\beta(x)$ and $\gamma(x)$, as shown. σ_x is the characteristic width of a solute zone and $U(x)$ is the area-averaged axial velocity distribution.

also present a closed-form analytical description of the physical regimes of positive versus negative variance growth. To further demonstrate the utility of the analysis, we engineer two channel geometries of specialized functions. The first geometry results in a constant variance and the second results in a sinusoidal variance in space.

2 Theory

2.1 Taylor-Aris dispersion in arbitrarily shaped cylinders

We analyze Taylor-Aris dispersion for flow in an axisymmetric channel with a slowly varying, arbitrary radius $a = a(x)$. We define variables for the first and second derivatives as $\beta(x) = da/dx$ and $\gamma(x) = d^2a/dx^2$. Given the azimuthal symmetry, the concentration $c(x, r, t)$ of a solute evolves according to the following convection-diffusion equation in cylindrical coordinates.

$$\frac{\partial c}{\partial t} + u_r \frac{\partial c}{\partial r} + u_x \frac{\partial c}{\partial x} = D \left(\frac{1}{r} \frac{\partial}{\partial r} \left(r \frac{\partial c}{\partial r} \right) + \frac{\partial^2 c}{\partial x^2} \right) \quad (1)$$

For the velocity field, we make the assumptions typical of lubrication theory of a slowly varying radius with a gap height much smaller than the axial distance of interests.⁷ Hence we write the velocity field based as

$$u_x(x, r) = 2U(x) \left(1 - \frac{r^2}{a(x)^2}\right), \quad u_r(x, r) = 2\beta(x)U(x) \left(\frac{r}{a(x)} - \frac{r^3}{a(x)^3}\right)$$

For the Taylor-Aris analysis, we follow the notation of Stone and Brenner⁸ and decompose variables into cross-sectional averages of the form $\langle(\cdot)\rangle \equiv \frac{1}{\pi a(x)^2} \int_0^{a(x)} 2\pi r(\cdot)dr$ and deviations therefrom defined as $(\cdot)' \equiv (\cdot) - \langle(\cdot)\rangle$. Hence, the known velocity field becomes

$$\langle u_x \rangle = U(x), \quad \langle u_r \rangle = \frac{8}{15}\beta(x)U(x)$$

$$u'_x = U(x) \left(1 - \frac{2r^2}{a(x)^2}\right), \quad u'_r = 2\beta(x)U(x) \left(\frac{r}{a(x)} - \frac{r^3}{a(x)^3} - \frac{4}{15}\right)$$

We then expand the convective-diffusion equation as

$$\begin{aligned} \frac{\partial \langle c \rangle}{\partial t} + \frac{\partial c'}{\partial t} + \langle u_r \rangle \frac{\partial c'}{\partial r} + u'_r \frac{\partial c'}{\partial r} + U \frac{\partial \langle c \rangle}{\partial x} + U \frac{\partial c'}{\partial x} + u'_x \frac{\partial \langle c \rangle}{\partial x} + u'_x \frac{\partial c'}{\partial x} \\ = D \left(\frac{1}{r} \frac{\partial}{\partial r} \left(r \frac{\partial c'}{\partial r} \right) + \frac{\partial^2 \langle c \rangle}{\partial x^2} + \frac{\partial^2 c'}{\partial x^2} \right) \end{aligned} \quad (2)$$

The area-average of the latter equation is then

$$\begin{aligned} \frac{\partial \langle c \rangle}{\partial t} + \langle u_r \rangle \left\langle \frac{\partial c'}{\partial r} \right\rangle + \left\langle u'_r \frac{\partial c'}{\partial r} \right\rangle + U \frac{\partial \langle c \rangle}{\partial x} + U \left\langle \frac{\partial c'}{\partial x} \right\rangle + \left\langle u'_x \frac{\partial c'}{\partial x} \right\rangle \\ = D \left(\left\langle \frac{1}{r} \frac{\partial}{\partial r} \left(r \frac{\partial c'}{\partial r} \right) \right\rangle + \frac{\partial^2 \langle c \rangle}{\partial x^2} + \left\langle \frac{\partial^2 c'}{\partial x^2} \right\rangle \right) \end{aligned} \quad (3)$$

We note there are here five additional terms that do not show up in the analysis of Taylor-Aris dispersion in cylinder of constant radius. We evaluate these using Leibniz's rule, integration by

parts, and chain rule as follows:

$$\begin{aligned}\left\langle \frac{\partial c'}{\partial r} \right\rangle &= \frac{1}{a(x)^2} \int_0^{a(x)} 2r \frac{\partial c'}{\partial r} dr = \frac{2}{a(x)^2} \int_0^{a(x)} \left(\frac{\partial}{\partial r} (rc') - c' \right) dr \\ &= \frac{2}{a(x)^2} \left(ac'(a) - \int_0^a c' dr \right)\end{aligned}$$

$$\begin{aligned}\left\langle \frac{\partial c'}{\partial x} \right\rangle &= \frac{1}{a(x)^2} \int_0^{a(x)} 2r \frac{\partial c'}{\partial x} dr = \frac{2}{a(x)^2} \int_0^{a(x)} \frac{\partial (rc')}{\partial x} dr \\ &= \frac{2}{a(x)^2} \left[\frac{d}{dx} \int_0^{a(x)} rc' dr - ac'(a)\beta(x) \right] = \frac{-2c'(a)\beta(x)}{a(x)}\end{aligned}$$

$$\begin{aligned}\left\langle \frac{1}{r} \frac{\partial}{\partial r} \left(r \frac{\partial c'}{\partial r} \right) \right\rangle &= \frac{2}{a(x)^2} \int_0^{a(x)} r \frac{1}{r} \frac{\partial}{\partial r} \left(r \frac{\partial c'}{\partial r} \right) dr = \frac{2}{a(x)^2} \left(a \frac{\partial c'}{\partial r} \Big|_{r=a} - 0 \right) \\ &= \frac{2}{a} \frac{\partial c'}{\partial r} \Big|_{r=a}\end{aligned}$$

$$\begin{aligned}\left\langle \frac{\partial^2 c'}{\partial x^2} \right\rangle &= \frac{2}{a(x)^2} \int_0^{a(x)} r \frac{\partial^2 c'}{\partial x^2} dr = \frac{2}{a(x)^2} \int_0^{a(x)} \frac{\partial^2 (rc')}{\partial x^2} dr \\ &= \frac{2}{a^2} \left[\frac{d}{dx} \int_0^{a(x)} \frac{\partial (rc')}{\partial x} dr - \beta(x) \frac{\partial (ac'(a))}{\partial x} \right] \\ &= \frac{2}{a^2} \left[\frac{d}{dx} \left(\frac{d}{dx} \int_0^{a(x)} rc' dr - \beta(x) ac'(a) \right) - \beta(x) \frac{\partial (ac'(a))}{\partial x} \right] \\ &= -\frac{2\gamma c'(a)}{a} - \frac{4\beta}{a^2} \frac{\partial}{\partial x} (ac'(a))\end{aligned}$$

Inserting these terms to equation 3, we have

$$\begin{aligned}\frac{\partial \langle c \rangle}{\partial t} + \frac{2\langle u_r \rangle}{a^2} \left(ac'(a) - \int_0^a c' dr \right) + \left\langle u'_r \frac{\partial c'}{\partial r} \right\rangle + U \frac{\partial \langle c \rangle}{\partial x} - \frac{2Uc'(a)\beta(x)}{a(x)} + \left\langle u'_x \frac{\partial c'}{\partial x} \right\rangle \\ = \frac{2D}{a} \frac{\partial c'}{\partial r} \Big|_{r=a} + D \frac{\partial^2 \langle c \rangle}{\partial x^2} - \frac{4\beta D}{a^2} \frac{\partial}{\partial x} (ac'(a)) - \frac{2\gamma Dc'(a)}{a}\end{aligned}\quad (4)$$

Subtracting the averaged equation from Equation 2 yields the following equation for the deviation of concentration:

$$\begin{aligned}
& \frac{\partial c'}{\partial t} + \langle u_r \rangle \frac{\partial c'}{\partial r} - \frac{2\langle u_r \rangle}{a^2} \left(ac'(a) - \int_0^a c' dr \right) + u'_r \frac{\partial c'}{\partial r} - \left\langle u'_r \frac{\partial c'}{\partial r} \right\rangle \\
& + U \frac{\partial c'}{\partial x} + \frac{2Uc'(a)\beta(x)}{a(x)} + u'_x \frac{\partial \langle c \rangle}{\partial x} + u'_x \frac{\partial c'}{\partial x} - \left\langle u'_x \frac{\partial c'}{\partial x} \right\rangle \quad (5) \\
& = D \frac{1}{r} \frac{\partial}{\partial r} \left(r \frac{\partial c'}{\partial r} \right) - \frac{2D}{a} \frac{\partial c'}{\partial r} \Big|_{r=a} + D \frac{\partial^2 c'}{\partial x^2} + \frac{4\beta D}{a^2} \frac{\partial}{\partial x} (ac'(a)) + \frac{2\gamma D c'(a)}{a}
\end{aligned}$$

To determine the dominant terms on the left and right hand side of the equation, we perform a scaling analysis with the following scales: $\langle c \rangle = c_0 \langle c^* \rangle$, $c' = c'_0 c'^*$, $x = \sigma x^*$, $r = ar^*$, $\epsilon = a/\sigma$, $t = t_{\text{obs}} t^*$, $u'_x = U u'_x^*$, and $u_r = \beta U u_r^*$. Hence, the non-dimensional form of Equation 5 is then

$$\begin{aligned}
& \frac{c'_0}{t_{\text{obs}}} \frac{\partial c'^*}{\partial t^*} + \frac{\beta U c'_0}{a} \left(\langle u_r^* \rangle \frac{\partial c'^*}{\partial r^*} - 2\langle u_r^* \rangle \left(c'^*(1) - \int_0^1 c'^* dr^* \right) + u'_r{}^* \frac{\partial c'^*}{\partial r^*} - \left\langle u'_r{}^* \frac{\partial c'^*}{\partial r^*} \right\rangle \right) \\
& + \frac{U c_0}{\sigma} u'_x{}^* \frac{\partial \langle c^* \rangle}{\partial x^*} + \frac{2U\beta c'_0}{a} c'^*(1) + \frac{U c'_0}{\sigma} \left(\frac{\partial c'^*}{\partial x^*} + u'_x{}^* \frac{\partial c'^*}{\partial x^*} - \left\langle u'_x{}^* \frac{\partial c'^*}{\partial x^*} \right\rangle \right) \quad (6) \\
& = \frac{D c'_0}{a^2} \left(\frac{1}{r^*} \frac{\partial}{\partial r^*} \left(r^* \frac{\partial c'^*}{\partial r^*} \right) - 2 \frac{\partial c'^*}{\partial r^*} \Big|_{r^*=1} \right) + \frac{D c'_0}{\sigma^2} \frac{\partial^2 c'^*}{\partial x^{*2}} \\
& + \frac{4\beta D c'_0}{a\sigma} \frac{\partial c'^*(r^*=1)}{\partial x^*} + \frac{2\gamma D c'_0}{a} c'^*(r^*=1)
\end{aligned}$$

We define σ as the characteristic axial dimension of the solute zone, and t_{obs} as the characteristic time over which the solute is observed. Our scaling assumes the geometrical ratio $\epsilon = a/\sigma$ as a primary smallness parameter ($\epsilon \ll 1$). We also assume the characteristic advection time (e.g. over the characteristic length σ) is much smaller than the diffusion time over the characteristic radius. Hence, we assume that $Ua^2/(\sigma D) = \epsilon Pe_a$, is small (e.g. order ϵ or smaller). Further, c_0 and c'_0 are the characteristic scales of the area-averaged solute concentration and its deviation, respectively, and we assume c'_0/c_0 is order ϵ . Consistent with our assumption of slowly varying radius, we further assume β and $\gamma\sigma$ are each order ϵ or smaller. Consistent with a Taylor-Aris dispersion regime, this scaling results in an approximate balance between the advective dispersion term and

the radial diffusion term as

$$u'_x \frac{\partial \langle c \rangle}{\partial x} = D \frac{1}{r} \frac{\partial}{\partial r} \left(r \frac{\partial c'}{\partial r} \right) - \frac{2D}{a} \frac{\partial c'}{\partial r} \Big|_{r=a} \quad (7)$$

Next, we consider the boundary condition on the inner wall of the channel. We impose a no flux boundary condition at each axial location along the wall, $\nabla c \cdot \hat{n} = 0$. This requires $-\frac{\partial c}{\partial r} \Big|_{r=a} + \beta \frac{\partial c}{\partial x} \Big|_{r=a} = -\frac{\partial c'}{\partial r} \Big|_{r=a} + \beta \frac{\partial \langle c \rangle}{\partial x} \Big|_{r=a} + \beta \frac{\partial c'}{\partial x} \Big|_{r=a} = 0$. Hence, we can express the radial diffusion terms as follows

$$\begin{aligned} D \frac{1}{r} \frac{\partial}{\partial r} \left(r \frac{\partial c'}{\partial r} \right) - \frac{2D}{a} \frac{\partial c'}{\partial r} \Big|_{r=a} &= D \frac{1}{r} \frac{\partial}{\partial r} \left(r \frac{\partial c'}{\partial r} \right) - \frac{2D\beta}{a} \left(\frac{\partial \langle c \rangle}{\partial x} \Big|_{r=a} + \frac{\partial c'}{\partial x} \Big|_{r=a} \right) \\ &\approx D \frac{1}{r} \frac{\partial}{\partial r} \left(r \frac{\partial c'}{\partial r} \right) - \frac{2D\beta}{a} \frac{\partial \langle c \rangle}{\partial x} \Big|_{r=a} \end{aligned}$$

The approximate equality here reflects that the axial gradients of c' are much smaller than those of $\langle c \rangle$. Substituting this evaluation into Equation 7, we have

$$D \frac{1}{r} \frac{\partial}{\partial r} \left(r \frac{\partial c'}{\partial r} \right) \approx u'_x \frac{\partial \langle c \rangle}{\partial x} + \frac{2D\beta}{a} \frac{\partial \langle c \rangle}{\partial x} \Big|_{r=a} \approx u'_x \frac{\partial \langle c \rangle}{\partial x} \quad (8)$$

The second equality above is obtained after assuming a small rate of change in radius compared to the Peclet number based on local radius such that $\beta \ll \frac{Ua}{D} = Pe_a$.

As typical of Taylor-Aris analyses, we then directly integrate Equation 8 as

$$r \frac{\partial c'}{\partial r} = \frac{\partial \langle c \rangle}{\partial x} \frac{U(x)}{D} \left(\frac{r^2}{2} - \frac{r^4}{2a^2} + c_1(x, t) \right)$$

Here, the function $c_1(x, t)$ results from the partial integration with respect to r . Evaluating this expression at $r = 0$, we see $r \frac{\partial c'}{\partial r} \Big|_{r=0} = c_1 \frac{\partial \langle c \rangle}{\partial x} \frac{U(x)}{D} = 0$, whence $c_1(x, t) = 0$. Integrating the equation a second time we obtain

$$c' = \frac{\partial \langle c \rangle}{\partial x} \frac{U(x)}{D} \left(\frac{r^2}{4} - \frac{r^4}{8a^2} + c_2(x, t) \right)$$

By the definition of the fluctuating quantity, $\int_0^a r c' dr = 0$. We use this to solve for c_2 and obtain an expression of c'

$$c'(x, r, t) = \frac{\partial \langle c \rangle}{\partial x} \frac{U(x)}{D} \left(\frac{r^2}{4} - \frac{r^4}{8a^2} - \frac{a^2}{12} \right) \quad (9)$$

We next differentiate this expression with respect to x , multiply by the known function u'_x , and take an area integral to construct the term $\langle u'_x \frac{\partial c'}{\partial x} \rangle$. We perform similar procedures for the second, third, and fifth terms of the left-hand side (LHS) and the first, third and fourth terms of the right-hand side (RHS) of Eq. 4. This yields the following expression for the development of the area-averaged concentration:

$$\frac{\partial \langle c \rangle}{\partial t} + U \left(1 + \frac{1}{6} \beta(x)^2 + \frac{1}{12} a(x) \gamma(x) \right) \frac{\partial \langle c \rangle}{\partial x} = D \left(1 + \frac{1}{48} \frac{U^2 a^2}{D^2} - \frac{1}{6} \frac{U a}{D} \beta(x) \right) \frac{\partial^2 \langle c \rangle}{\partial x^2} \quad (10)$$

Note that, for $\beta = \gamma = 0$, Equation 10 reduces to the simple result of Taylor-Aris dispersion for a uniform-radius cylinder.³

In the next section, we will use Equation 10 to develop a description of the development of the axial mean position of the solute and its axial variance. For now, we note the right-hand side of Equation 10 contains a prefactor for the second axial derivative $\frac{\partial^2 \langle c \rangle}{\partial x^2}$ which has the form of a typical Taylor-Aris dispersion coefficient:

$$D_{\text{eff}} \equiv D \left(1 + \frac{1}{48} \frac{U^2 a^2}{D^2} - \frac{1}{6} \frac{U a}{D} \beta \right) \quad (11)$$

However, as we will discuss in the following sections, the coefficient D_{eff} is by itself not useful in predicting the time evolution of variance. This is true even for the simple case of linearly converging or diverging channel (i.e., $\beta = \text{Constant}$). The reason for this is that development of the solute zone variance is a strong function of the advective operator on the left-hand side. These advective gradients can stretch or shrink the variance as the solute navigates through contractions and expansions, respectively.

2.2 Time evolution of mean and variance

We next formulate the problem in terms of analytical expressions of two moments of solute distributions. Note that, despite this use of spatial moments, our analysis does not follow Aris' famous method of moments³ as we here focus on the mean and variance of the solute distribution in the typical Taylor-Aris limit where observation times are much longer than the radial diffusion time. Our analysis also uses scaling analyses and approximations for key terms which are not part of the method of moments.

We first define an axial average as

$$\overline{(\cdot)} \equiv \int_{-\infty}^{\infty} (\cdot) \langle c \rangle(x', t) dx' / \int_{-\infty}^{\infty} \langle c \rangle(x', t) dx',$$

where x' is a dummy variable for integration. For more compact notation, we also define \bar{c} as the axial integration of the mean concentration $\int_{-\infty}^{\infty} \langle c \rangle(x', t) dx' \equiv \bar{c} = \bar{c}(t)$.

To derive an expression for \bar{c} , we directly integrate Equation 10 with respect to x :

$$\int_{-\infty}^{\infty} \frac{\partial \langle c \rangle}{\partial t} dx + \int_{-\infty}^{\infty} U \left(1 + \frac{\beta^2}{6} + \frac{a\gamma}{12} \right) \frac{\partial \langle c \rangle}{\partial x} dx = \int_{-\infty}^{\infty} D \left(1 + \frac{1}{48} \frac{U^2 a^2}{D^2} - \frac{1}{6} \frac{U a}{D} \beta \right) \frac{\partial^2 \langle c \rangle}{\partial x^2} dx$$

We evaluate integrals using integration by parts, divide both sides with \bar{c} , and hence arrive at an ODE for (zeroth moment) $\bar{c}(t)$:

$$\frac{d \ln \bar{c}}{dt} = U_0 a_0^2 \overline{\frac{d}{dx} \left[\frac{1 + \beta^2/6 + a\gamma/12}{a^2} \right]} + D \left[\frac{U_0^2 a_0^4}{48 D^2} \overline{\frac{d^2}{dx^2} \left(\frac{1}{a^2} \right)} - \frac{U_0 a_0^2}{6 D} \overline{\frac{d^2}{dx^2} \left(\frac{\beta}{a} \right)} \right] \quad (12)$$

We apply a similar procedure to derive the first moment. That is, we multiply Equation 10 with x , apply the axial average operation $\overline{(\cdot)}$, and arrive at an ODE for the axial mean position $\bar{x}(t)$ as

follows:

$$\begin{aligned}
\bar{x} \frac{d \ln \bar{c}}{dt} + \frac{d\bar{x}}{dt} &= U_0 a_0^2 \left[\frac{1 + \beta^2/6 + a\gamma/12}{a^2} + x \frac{d}{dx} \left[\frac{1 + \beta^2/6 + a\gamma/12}{a^2} \right] \right] \\
&+ 2D \left[\frac{U_0^2 a_0^4}{48D^2} \frac{d}{dx} \left(\frac{1}{a^2} \right) - \frac{U_0 a_0^2}{6D} x \frac{d}{dx} \left(\frac{\beta}{a} \right) \right] \\
&+ D \left[\frac{U_0^2 a_0^4}{48D^2} x \frac{d^2}{dx^2} \left(\frac{1}{a^2} \right) - \frac{U_0 a_0^2}{6D} x \frac{d^2}{dx^2} \left(\frac{\beta}{a} \right) \right]
\end{aligned} \tag{13}$$

Note that this equation contains (on the right-hand side) an expression of the form $\overline{xf(x)}$. Some analysis of this term is essential for further analytical simplification of the problem. We therefore consider a Taylor expansion of $xf(x)$ about the mean axial position \bar{x} as follows:

$$xf(x) = \bar{x}f(\bar{x}) + (x - \bar{x})(\bar{x}f'(\bar{x}) + f(\bar{x})) + (x - \bar{x})^2 \left(\frac{1}{2} \bar{x}f''(\bar{x}) + f'(\bar{x}) \right) + \dots$$

To derive an approximate formulation for $\overline{xf(x)}$, we will assume that the axial distribution of mean concentration is roughly a Gaussian distribution. With the latter assumption, the term $(x - \bar{x})(\bar{x}f'(\bar{x}) + f(\bar{x}))$ vanishes after an axial integration. Then, as long as $\bar{x}f(\bar{x}) \gg \sigma_x^2 \left(\frac{1}{2} \bar{x}f''(\bar{x}) + f'(\bar{x}) \right)$, where $\sigma_x^2 = \overline{(x - \bar{x})^2}$ is the axial variance of solute, we can approximate $\overline{xf(x)} \approx \bar{x}f(\bar{x})$. We consider this treatment of the solute shape (as a Gaussian) as a useful heuristic. We shall later show that, in the Taylor-Aris regime, the exact distribution of the area-averaged concentration is very close to a Gaussian with negligible skewness and negligible excess kurtosis. We repeat this heuristics for all $\overline{(\cdot)}$ terms in the first moment equation (Eq. 13), subtract the zeroth moment equation from it, and thereby derive the following ODE for $\bar{x}(t)$:

$$\frac{d\bar{x}}{dt} \approx U_0 a_0^2 \left[\frac{1 + \beta^2/6 + a\gamma/12}{a^2} \right] + D \left[\frac{U_0^2 a_0^4}{48D^2} \frac{d}{dx} \left(\frac{1}{a^2} \right) - \frac{U_0 a_0^2}{6D} \frac{d}{dx} \left(\frac{\beta}{a} \right) \right], \tag{14}$$

where $\tilde{f} \equiv f(\bar{x})$.

To derive the second moment equation of Equation 10, we multiply Equation 10 by $(x - \bar{x})^2$, directly integrate it with respect to x , perform integration by parts, and divide both sides by \bar{c} . This

then yields the following ODE for the dynamics of σ_x^2 :

$$\begin{aligned}
\sigma_x^2 \frac{d \ln \bar{c}}{dt} + \frac{d\sigma_x^2}{dt} = & -U_0 a_0^2 \left[\overline{(x - \bar{x})^2 \frac{d}{dx} \left[\frac{1 + \beta^2/6 + a\gamma/12}{a^2} \right]} + 2(x - \bar{x}) \left[\frac{1 + \beta^2/6 + a\gamma/12}{a^2} \right] \right] \\
& + 2D \left[1 + \frac{U_0^2 a_0^4}{48D^2} \overline{\left(\frac{1}{a^2} \right)} - \frac{U_0 a_0^2}{6D} \overline{\left(\frac{\beta}{a} \right)} \right] \\
& + D \left[\frac{U_0^2 a_0^4}{48D^2} \overline{(x - \bar{x})^2 \frac{d^2}{dx^2} \left(\frac{1}{a^2} \right)} - \frac{U_0 a_0^2}{6D} \overline{(x - \bar{x})^2 \frac{d^2}{dx^2} \left(\frac{\beta}{a} \right)} \right] \\
& + D \left[\frac{U_0^2 a_0^4}{12D^2} \overline{(x - \bar{x}) \frac{d}{dx} \left(\frac{1}{a^2} \right)} - \frac{2U_0 a_0^2}{3D} \overline{(x - \bar{x}) \frac{d}{dx} \left(\frac{\beta}{a} \right)} \right]
\end{aligned} \tag{15}$$

Note that the RHS of Equation 15 contains expressions of the form $\overline{f(x)}$, $\overline{(x - \bar{x})f(x)}$, and $\overline{(x - \bar{x})^2 f(x)}$. We again simplify these expressions using Taylor expansion at the mean axial position \bar{x} as follows:

$$\begin{aligned}
f(x) &= f(\bar{x}) + (x - \bar{x})f'(\bar{x}) + \frac{1}{2}(x - \bar{x})^2 f''(\bar{x}) + \dots \\
(x - \bar{x})f(x) &= (x - \bar{x})f(\bar{x}) + (x - \bar{x})^2 f'(\bar{x}) + \frac{1}{2}(x - \bar{x})^3 f''(\bar{x}) + \frac{1}{6}(x - \bar{x})^4 f'''(\bar{x}) \dots \\
(x - \bar{x})^2 f(x) &= (x - \bar{x})^2 f(\bar{x}) + (x - \bar{x})^3 f'(\bar{x}) + \frac{1}{2}(x - \bar{x})^4 f''(\bar{x}) + \dots
\end{aligned}$$

Again, we apply our assumption of an approximately Gaussian distribution, so that the terms with odd powers of $(x - \bar{x})$ vanish after an axial integration. Then as long as $f(\bar{x}) \gg \frac{1}{2}\sigma_x^2 f''(\bar{x})$, $\sigma_x^2 f'(\bar{x}) \gg \frac{1}{6}\overline{(x - \bar{x})^4} f'''(\bar{x})$, and $\sigma_x^2 f(\bar{x}) \gg \frac{1}{2}\overline{(x - \bar{x})^4} f''(\bar{x})$, we can approximate $\overline{f(x)} \approx f(\bar{x})$, $\overline{(x - \bar{x})f(x)} \approx \sigma_x^2 f'(\bar{x})$, and $\overline{(x - \bar{x})^2 f(x)} \approx \sigma_x^2 f(\bar{x})$, respectively. We substitute these expressions

into Equation 15 and arrive at an ODE of the axial variance $\sigma_x^2(t)$ as

$$\begin{aligned}
\frac{d\sigma_x^2}{dt} &\approx 2U_0a_0^2\sigma_x^2 \frac{d}{dx} \left[\frac{1 + \overline{\beta^2/6 + a\gamma/12}}{a^2} \right] \\
&+ 2D \left[1 + \frac{U_0^2a_0^4}{48D^2} \overline{\left(\frac{1}{a^2}\right)} - \frac{U_0a_0^2}{6D} \overline{\left(\frac{\beta}{a}\right)} \right] \\
&+ 5D\sigma_x^2 \left[\frac{U_0^2a_0^4}{48D^2} \frac{d^2}{dx^2} \overline{\left(\frac{1}{a^2}\right)} - \frac{U_0a_0^2}{6D} \frac{d^2}{dx^2} \overline{\left(\frac{\beta}{a}\right)} \right]
\end{aligned} \tag{16}$$

Equation 14 and 16 are two coupled ODEs that predict the time evolution of axial mean and variance of solute based on channel geometry alone. Here ends the primary analytical formulation that we will leverage in this work to describe the dynamics of the solute. In Section 3, we will use these two equations to predict the time evolution of the axial mean and variance of solute zone for various interesting channel geometries.

2.3 Analytical derivation of the boundary between the regimes of positive and negative growth of axial variance

Advective dispersion can cause the axial variance of the solute zone to decrease as the solute traverses a region where the channel is expanding. Such an expanding channel region can be, qualitatively, characterized by a positive and sufficiently large value of β , a sufficiently large Pe_a (so that axial diffusion does not completely overpower the advective effect), and a sufficiently small value of the axial variance relative to the local channel radius. We here explore this effect. Enabled by our analytical approach, we will formulate the boundary between the physical regimes of positive and negative growth of axial variance of the solute. To determine the dominant terms on the right-hand side of Equation 16, we first perform a scaling analysis. For this regime analysis, we will consider a geometry that varies with a characteristic length-scale or wavelength λ that is significantly greater than the radius a . Given this, we can evaluate the two ratios associated with

the three σ_x^2 -dependent terms as follows:

$$\frac{2U_0a_0^2\sigma_x^2\frac{d}{dx}\left[\frac{1+\beta^2/6+a\gamma/12}{a^2}\right]}{5D\sigma_x^2\frac{U_0^2a_0^4}{48D^2}\frac{d^2}{dx^2}\left(\frac{1}{a^2}\right)} \sim \frac{1/\lambda}{\frac{U_0a_0^2}{D}\frac{1}{\lambda^2}} \sim \frac{\lambda/a_0}{Pe_{a_0}}$$

$$\frac{2U_0a_0^2\sigma_x^2\frac{d}{dx}\left[\frac{1+\beta^2/6+a\gamma/12}{a^2}\right]}{5D\sigma_x^2\frac{U_0a_0^2}{6D}\frac{d^2}{dx^2}\left(\frac{\beta}{a}\right)} \sim \frac{\frac{1}{\lambda}\frac{1}{a^2}}{\frac{1}{\lambda^2}\frac{1}{a}} \sim \frac{\lambda}{a}$$

Whence, the scaling analysis suggests that, for $\lambda/a \gg 1$, $2U_0a_0^2\sigma_x^2\frac{d}{dx}\left[\frac{1+\beta^2/6+a\gamma/12}{a^2}\right]$ is the dominant variance-dependent term in Equation 16. This further suggests we can approximate the time evolution of variance for a slowly diverging channel where $\gamma = 0$ and $0 < \beta \ll \min(Pe_a^{-1}, 1)$ as follows

$$\frac{1}{D}\frac{d\sigma_x^2}{dt} \approx -4Pe_a\left(\frac{\sigma_x^2}{a^2}\right)\beta\left(1 + \frac{\beta^2}{6}\right) + 2\left[1 + \frac{1}{48}Pe_a^2 - \frac{1}{6}Pe_a\beta\right]. \quad (17)$$

This approximate expression then yields a closed-form description of the boundary between the regimes of positive and negative growth of axial variance in terms of β , Pe_a , and σ_x^2/a^2 .

Figure 2 shows a plot of this boundary as a three-dimensional surface in terms of the aforementioned three variables. That is, the surface (Fig. 2A) delineates the regions of positive and negative growth of axial variance as a function of local Peclet number (Pe_a), local slope of channel radius distribution (β), and local ratio between variance and squared radius (σ_x^2/a^2). Figure 2B shows the contours of horizontal cross-section of the surface for various values of $\ln(\sigma_x^2/a^2)$ (labeled on each contour line). Points above the surface exhibit a negative rate of axial variance growth, while points below have a positive rate of growth. Accordingly, the surface defines the solution for zero growth in variance in this three-parameter space. As expected, the surface asymptotes toward the Pe_a - β plane for finite Pe_a , small variances, and larger values of β . We also see that for fixed and finite values of (positive) β , the critical variance value σ_x^2/a^2 has a minimum as a function of Pe_a .

$$\frac{\sigma_x^2}{a^2} = \frac{1 + \frac{1}{48}Pe_a^2 - \frac{1}{6}Pe_a\beta}{2Pe_a\beta(1 + \beta^2/6)}$$

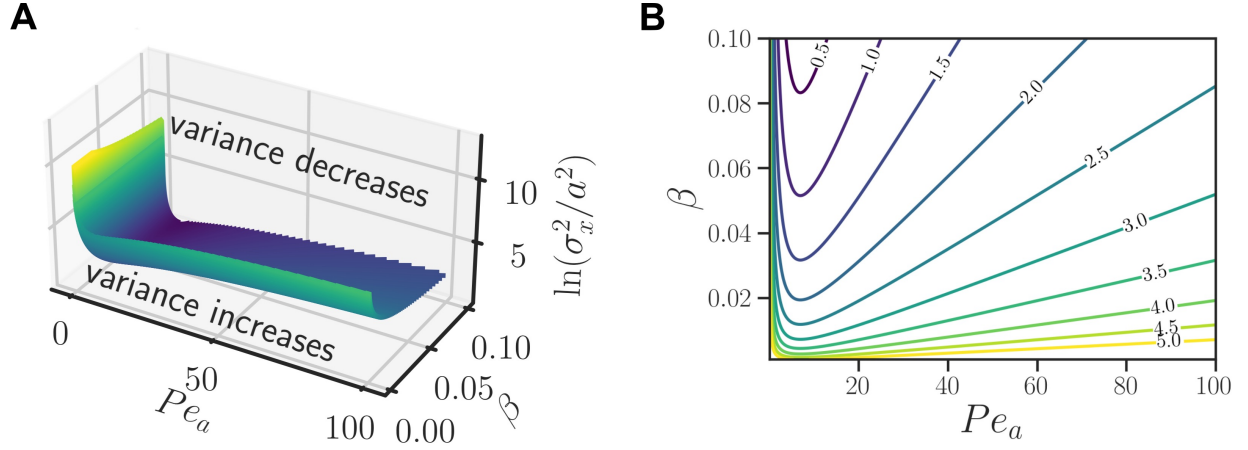


Figure 2: Regimes of positive and negative growth of axial variance of solute. (A) Surface of zero variance growth in a space of Peclet number, β , and the natural log of the local ratio between variance and squared radius ($\ln(\sigma_x^2/a^2)$). This surface is computed analytically (in closed form) from Equation 17. Shown is a surface where the variance rate of growth, $\frac{d\sigma_x^2}{dt}$, is approximately 0. (B) The contour plot shows the horizontal cross-section curves of the zero variance growth surface in a space of Peclet number, β , and $\ln(\sigma_x^2/a^2)$, at different $\ln(\sigma_x^2/a^2)$ values.

We differentiate the above expression with respect to Pe_a , set it equal to zero, and arrive at the minimal variance required for negative variance growth:

$$\min\left(\frac{\sigma_x^2}{a^2}\right) = \frac{1 - \beta/\sqrt{3}}{4\sqrt{3}\beta(1 + \beta^2/6)}.$$

The minimum variance occurs at $Pe_a = \sqrt{48}$.

2.4 Approximations useful for channel design

The closed-form analytical expression of Equation 17 is useful in engineering desired variance evolutions in the Taylor-Aris dispersion regime. We can simplify such a solution further by

implementing the following three approximations:

$$\begin{aligned}\frac{d}{dt} &\approx \frac{d}{dx} \frac{d\bar{x}}{dt} \\ \beta(1 + \beta^2/6) &\approx \beta \\ \frac{d\bar{x}}{dt} &\approx \frac{U_0 a_0^2}{a(\bar{x})}\end{aligned}$$

Inserting these three approximations into Equation 17, and substituting the definition of β , we obtain an ODE for $a(x)$ given a desired spatial distribution $\sigma_x^2(x)$:

$$\frac{da}{dx} \approx \frac{-\frac{d\sigma_x^2}{dx} + \frac{2a^2 D}{U_0 a_0^2} + \frac{U_0 a_0^2}{24D}}{\frac{4\sigma_x^2}{a} + \frac{a}{3}} \quad (18)$$

We can then numerically solve Equation 18 to obtain the shape of the engineered channel. In Section 3.4, We will use this approximation to design channels that can result in specific variance evolution pattern in space.

2.5 Brownian Dynamics simulations

We used Brownian dynamics simulations to benchmark and evaluate our analytical expressions for variance evolution. Each Brownian dynamics simulation consisted of tracking 5,000 point-particles which were initially uniformly distributed along the radius and normally distributed along the streamwise direction. We considered a mean axial position of 0 (by definition) and an initial axial variance of $\sigma_{x,0}^2$. We set $\sigma_{x,0}^2 = 300a_0^2$ for the two engineered channels in Section 3.4, and we set $\sigma_{x,0}^2 = 10a_0^2$ for all other cases.

For the time steps, we set the ratio between diffusion time scale (a_0^2/D) to time step of discretization to 40. Each reflection at the wall was checked twice at each time step. Unless specified, the (constant, initial) Peclet number based on initial radius (Pe_{a_0}) was 10. Five simulations from different random seed initial conditions were computed for each case, and the reported values are their average. The program was written in Python 3 and is available on

Github(jrchang/Taylor_dispersion_arbitrary).

2.6 A note on naive estimation of variance

We will perform a few comparisons of our solutions to a naive estimation based on the effective dispersion coefficient of the governing PDE. This is the (local) D_{eff} value which is defined in Equation 11. A naive prediction of dispersion in some system is defined here as a simple time integration of the variance weighted by the local D_{eff} value as follows:

$$\sigma_{x,\text{naive}}^2 = \sigma_x^2(t=0) + \int_0^t 2D_{\text{eff}}(x = \bar{x}(t))dt \quad (19)$$

We will show in Section 3 that results computed from this naive approximation are very often highly inaccurate. Also, as expected, this expression cannot predict any negative variance growth due to expanding channel regions.

3 Results and Discussion

3.1 Diverging and converging conical channels

We first apply our analysis to a simple case of diverging and converging conical section channels. Figures 3A and 3B shows solutions for dispersion of a solute zone in linearly diverging and converging channels, respectively. The top two figures in Figure 3 show particle zones at five non-dimensional times $2Dt/a_0^2$ (from 5 to 800) as they migrate through the channels. The axes are non-dimensionalized coordinates $r^* = r/a_0$ and $x^* = x/a_0$. Note the intensely exaggerated height-to-length aspect ratio of the figures, chosen here for clarity of presentation. The top half of the solute concentration in the channel are raw data results of the three-dimensional Brownian dynamics simulations. The bottom half of the channels show the (one-dimensional) area-averaged axial distribution of concentration of solute from the model developed here (i.e. numerical solutions of ODEs given by Eqs.14 and 16). The solute is initially uniformly distributed over the cross-

sectional area of the channel, and the initial standard deviation width of the axial solute distribution are each set equal to the same value (equal to $\sqrt{10}a_0 = \sqrt{10}a(x=0)$ of the diverging channel). The current model has very good comparison with the Brownian dynamics simulations. The characteristic Pe_a values here are order $O(10)$ and this results in negligible radial gradients of particle density in the Brownian dynamics. Hence, the particle clouds from Brownian dynamics are fairly symmetric about x^* . We plot the skewness and excess kurtosis of the particle clouds from Brownian dynamics simulation in Supplementary Figure S1. In both diverging and converging conical section channels, the skewness and excess kurtosis are very close to 0, confirming that the axial distribution of particle cloud is roughly a normal distribution. Note the general trend of relatively rapid increase of zone variance in the converging case. By comparison, the expansion in the diverging channel limits the growth of variance. For this case, the divergence is not sufficiently pronounced to result in negative growth of variance (but we shall explore such cases later below.)

The bottom two plots in Figure 3 are plots of the variance of the area-averaged axial distribution of solute concentration from the current model ($\sigma_{x,\text{curr}}^{*2}$), Brownian dynamics ($\sigma_{x,\text{B}}^{*2}$), and the naive estimation ($\sigma_{x,\text{naive}}^{*2}$). These quantities are plotted as a function of the axial mean position of solute zone, \bar{x}^* . There is excellent agreement between the current model and the Brownian dynamics simulation for both the diverging and converging cases. The naive model captures the initial slope of the curves but quickly diverges from the other two solutions. The naive model grossly over-predicts and under-predicts the long-term dispersion of the solute. The failure of the naive model is interesting as previous dispersion studies (e.g. Bryden and Brenner⁴) have analyzed local dispersion rates of such channels but not the long-term development of the solute. Our study is the first to predict the complete spatial evolution pattern of variance, and it is very clear that estimates based on simple time integration of local dispersion coefficients are highly inaccurate.

3.2 Periodic channels

We next apply our model to a periodic channel with sinusoidal radius distribution. Similar to the top plots of Figure 3, the top plot of Figure 4 shows a plot of the channel geometry in coordinates of

r^* versus x^* in a highly exaggerated aspect ratio for clarity. We show results for Pe_{a_0} of 10 where a_0 is defined as the radius at $x = 0$ and is also the axially averaged radius. Again, the channel shows plots of solute zones at non-dimensional times ranging from 5 to 800. The top half of the solute zones are raw results from the Brownian dynamics simulations, while the bottom half are plots of the predicted axial distribution of area-averaged concentration from the current model. Again, we see agreement between the axial distributions of Brownian dynamics particle densities and the axial distributions from the model. Note how the model captures the strongly positive and negative growth of variance as the solute traverses through contractions and expansions, respectively. For example, note the rapid increases in variance due to the contraction just upstream of $x^* = 1800$, and then the subsequent rapid decrease in variance caused by the advective effects of the solute expanding from $x^* = 1800$ to just upstream of $x^* = 3000$. Note that the particle clouds from Brownian dynamics are also fairly symmetric about x^* . In Supplementary Figure S2, we again plot the skewness and excess kurtosis of the particle clouds from Brownian dynamics simulation, showing that the skewness and excess kurtosis remain close to 0. This again confirms that the axial distribution of the solute cloud is roughly a normal distribution.

The bottom plot of Figure 4 shows the variance of the solute zone as a function of solute average axial location \bar{x}^* . Plotted are the variance from the Brownian dynamics simulation and the current model. Note the excellent agreement between these two models showing how the current model captures very well the detailed development of the variance. Note also how the variance at equal values of the phase increases and the variance averaged over the period increases monotonically. At the end of the current section, we will consider this development further and use our model to analyze period-averaged variance over long times.

Figure 4 also shows the non-dimensional area-averaged flow velocity and the local normalized effective dispersion coefficient, D_{eff}/D (c.f. two ordinances on the right-hand side of the plot). Both U and D_{eff}^* are periodic functions, antiphase to the shape of the channel. D_{eff}^* increases as the channel contracts and decreases as the channel expands, as we expected. However, even when the variance is actually decreasing (e.g. between $x^* = 2000$ to 3000) the effective dispersion coefficient

D_{eff}/D remains positive and greater than unity. This again demonstrates the inability of effective dispersion coefficient to describe the variance evolution (including here in a periodic channel).

We next consider the long-term averaged dispersion coefficient in periodic channels. As with previous studies of dispersion,^{5,6} we will define a new effective dispersion coefficient for the long-term (many period) growth of the variance D_{eff}^{∞} defined as follows:

$$D_{\text{eff}}^{\infty} \equiv \lim_{t \rightarrow \infty} \frac{\sigma_x^2}{2t}$$

The non-dimensional version of this quantity will be defined as $D_{\text{eff}}^{\infty*} \equiv D_{\text{eff}}^{\infty}/D$. We analyzed long-term dispersion behavior in periodic channels with three different shapes but with the same period and similar radius amplitude. Figure 5 summarizes the results of this study. The three plots in the top row show plots of the radius distribution $a(x)$ normalized by initial radius a_0 as a function of the normalized axial coordinate x^* . The three functions $a(x)$ are sinusoidal, triangular, and exponential-sine-wave functions of the following forms:

$$\begin{aligned} a_1(x) &= 1 + \delta \sin(2\pi x/\lambda) \\ a_2(x) &= 1 + \frac{3\delta}{2\lambda} \text{mod}(x, \lambda) - \frac{9\delta}{2\lambda} (\text{mod}(x, \lambda) - \frac{2}{3}\lambda) H(\text{mod}(x, \lambda) - \frac{2}{3}\lambda) \\ a_3(x) &= \frac{\delta}{e} \exp(\sin(2\pi x/\lambda)) + (1 - \frac{\delta}{e}), \end{aligned}$$

where $H(x)$ is the Heaviside step function. The three plots in the second row of Figure 5 show the effective, long-term dispersion coefficient $D_{\text{eff}}^{\infty*}$ for each case as a function of Pe_{a_0} . $D_{\text{eff}}^{\infty*}$ curves are shown for the current model (data point) and Brownian simulations (solid line). We see excellent agreement between the current model and the Brownian simulations for the long-term dispersion coefficient. The results capture an asymptote of $D_{\text{eff}}^{\infty*} = 1$ for vanishing Pe_{a_0} , as expected. $D_{\text{eff}}^{\infty*}$ increases monotonically with increasing Pe_{a_0} and asymptotes to a $Pe_{a_0}^2$ dependence for large Pe_{a_0} .

In the left-hand plot of the bottom row, we also show a comparison of our model results with the work of Adrover et al.⁶ Adrover analyzed the long-term dispersion of solutes in a sinusoidal channel and provided an approximate analytical formula for $D_{\text{eff}}^{\infty*}$ as a function of Pe_{a_0} , and this

prediction is plotted along with our model in the figure. Adrover's also found that $D_{\text{eff}}^{\infty*}$ tends to unity for small Pe_{a_0} and scales with the second power of Pe_a for large Pe_a . We note the excellent agreement among the three predictions.

We conclude the current model can be readily adapted to a wide variety of periodic channel shapes. We further note the similarity among the three $D_{\text{eff}}^{\infty*}$ versus Pe_{a_0} curves for the three cases. This similarity leads us to hypothesize that the long-term solute dispersion in such periodic channels is largely driven by the spatial frequency and the amplitude of the radius oscillation (and Pe_{a_0}) and may be insensitive to the details of channel shapes.

3.3 Arbitrarily-shaped channels

We next demonstrate a novel application of our model to some arbitrarily-shaped axisymmetric channel. Similar to the top plot of Figure 4, the top plot of Figure 6 shows a plot of the channel geometry in coordinates of r^* versus x^* in a highly exaggerated aspect ratio for clarity. We show results for Pe_{a_0} of 10 where a_0 is the radius at $x = 0$. The channel shows plots of solute zones at non-dimensional times ranging from 25 to 250. The top half of the solute zones are raw results from the Brownian dynamics simulations, while the bottom half are plots of the predicted axial distribution of area-averaged concentration from the current model. Again we see excellent agreement between the axial distributions of Brownian dynamics particle densities and the axial distributions from the model. Note how the model captures the sudden positive and negative growth of variance as the solute traverses through contractions and expansions, respectively. For example, note the sudden decreases in variance due to the expansion just upstream of $x^* = 500$, and then the sudden increases in variance caused by the contraction near $x^* = 700$.

The middle plot of Figure 6 shows the variance of the solute zone as a function of nondimensional solute average axial location, \bar{x}^* . Plotted are the variance from the Brownian dynamics simulation and the current model. Note the excellent agreement between these two models again showing how the current model captures very well the detailed development of the variance. For example, note the sudden decreases of variance just upstream of $x^* = 500$ and $x^* = 800$, and the sudden increases

of variance just upstream of $x^* = 700$.

The middle plot of Figure 6 also shows the non-dimensional area-averaged flow velocity and the local normalized effective dispersion coefficient, D_{eff}/D (c.f. two ordinances on the right-hand side). Similar to the case in Figure 4, both U and D_{eff}^* show opposite trend to the shape of the channel. D_{eff}^* again increases as the channel constricts and decreases as the channel expands, as we expected. However, even in a region where variance is decreasing (e.g. between $x^* = 400$ to 500), the effective dispersion coefficient remains positive and greater than unity. This again highlights the inability of effective dispersion coefficient to describe the variance evolution (i.e. the inability of the naive solution), here in an arbitrarily-shaped axisymmetric channel.

The bottom plot of Figure 6 shows the scaled rate of change of variance ($\frac{1}{D} \frac{d\sigma_x^2}{dt}$) as a function of solute average axial location \bar{x}^* . Plotted are the results computed from Brownian simulations, the current model (Eq.16), and the approximated closed-form introduced in Sec 2.3 (Eq.17). For the Brownian dynamics simulation, both raw data and the moving-averaged results are shown. The variance growth rate varies according to the geometry of the channel (shown in the top plot of the same figure), decreasing when the channel expands and increasing when the channel contracts, as we expect. There is also excellent agreement among the three solutions, and both the current model and approximated closed form captured the negative variance growth rate near $\bar{x}^* = 400$ and $\bar{x}^* = 700$. This shows the capability of our model to predict the variance evolution, and also provides validation of using Equation 17 to identify the regime of negative variance growth.

3.4 Engineering channel shape for specific variance patterns

Furthermore, we apply our closed-form analytical approach to design the channel shape to have a desired spatial evolution of variance. As a proof of concept, we design one channel that maintains an approximately constant variance (channel A) and another channel that results in a sinusoidal variation of variance as the solute develops in the channel (channel B).

The two channel shapes are designed by solving Equation 18. The shape of channel A monotonically diverges, and the rate of diverging increases downstream. For channel B, there is an increased

diverging rate between $x^* = 300$ and 500, coinciding with the region where it is necessary to reduce the variance according to the targeted sinusoidal pattern. Note that the channel shape in Figure 7A has an analytical expression. By setting the $\frac{d\sigma_x^2}{dx}$ term on the right-hand side of Equation 18 to 0, we can simplify Equation 18 into the following ODE for $a(x)$:

$$\frac{da}{dx} \approx \frac{\frac{6D}{U_0 a_0^2} \left(a + \frac{U_0^2 a_0^4}{48D^2} \frac{1}{a} \right)}{1 + 12\sigma_x^2 \frac{1}{a^2}}, \quad (20)$$

which has an analytical solution as follows:

$$c_1 + \frac{6D}{U_0 a_0^2} x = \frac{12\sigma_x^2}{\frac{U_0^2 a_0^4}{48D^2}} \log(a) + \frac{\frac{U_0^2 a_0^4}{48D^2} - 12\sigma_x^2}{2 \frac{U_0^2 a_0^4}{48D^2}} \log\left(a^2 + \frac{U_0^2 a_0^4}{48D^2}\right), \quad (21)$$

where c_1 is the constant of integration related to the initial variance. We know of no analytical closed-form solution for channel B.

Figures 7A and 7B show solutions for dispersion of solute zone in the two engineered channels. The channel in Figure 7A (abbreviated as "channel A") is designed to maintain an approximately constant variance of 300 ($\sigma_x^{2*}(\bar{x}^*) = 300$), while the channel in Figure 7B (abbreviated as "channel B") is designed to yield a sinusoidal axial variation of variance ($\sigma_x^{2*}(\bar{x}^*) = 300 + 50 \sin(2\pi\bar{x}^*/600)$). Similar to the top plot of Figure 3, the top two plots of Figure 7 shows the two engineered channel geometry in coordinates of r^* versus x^* . We show results for Pe_{a_0} of 10 where a_0 is taken as the radius at $x = 0$. The top half of the solute concentration in the channel are raw data results from Brownian dynamics simulations, while the bottom half of the channels show the area-averaged axial distribution of solute concentration predicted from the current model.

The bottom two plots in Figure 7 are plots of the variance of the area-averaged axial distribution of solute concentration from the current model ($\sigma_{x,\text{curr}}^{*2}$), Brownian dynamics ($\sigma_{x,\text{B}}^{*2}$), and the targeted variance spatial evolution pattern ($\sigma_{x,\text{target}}^{*2}$). These quantities are plotted as a function of the axial mean position of the solute zone, \bar{x}^* . For channel A, there is a near perfect agreement among the current model, Brownian dynamics simulation, and targeted pattern. All three lines stay flat

at variance of 300 as we expected. For channel B, there is a good agreement among the three quantities. Although the amplitude of the sinusoidal variation is slightly smaller compared to the targeted pattern, the Brownian dynamics simulation results show the desired sinusoidal spatial evolution pattern. To our knowledge, our study is the first to demonstrate the design of a channel shape that yields a desired spatial evolution pattern of variance. Without the analytical approach described in Section 2.2-2.4, this process would require repetitive simulation efforts (as with shape optimization) to compute channel shapes to obtain the desired pattern.

4 Summary and conclusions

We demonstrated a Taylor-Aris dispersion analysis for axisymmetric channels with slowly-varying, arbitrary radius distributions. We first derived a PDE for the development of the area-averaged concentration including an explicit, closed-form local dispersion coefficient. We then derived equations for the dynamics of the axial mean (first moment) and variance (second moment) of the solute distribution. The latter derivation was accomplished by performing further Taylor-Aris type scaling analysis and introducing smallness parameters based on the first and second derivative of the radius profile. We then approximated the shape of the area-averaged solute distribution as normal (Gaussian) distribution and proposed two heuristics for relations describing the moments of local geometry experienced by the solute. Our analysis allowed us to simplify the solution for the complex dynamics of solute zones to two coupled ODEs for the mean and variance. These ODEs provide a description of solute position and variance solely from the channel geometry. To our knowledge, this is the first time a full prediction of the time evolution of variance is possible (using only two ODEs) for this kind of problem.

We further derived a closed-form expression which delineates the regimes of positive and negative variance growth. This expression quantifies the solution of zero growth variance as a function of local Peclet number, local slope in the channel, and the ratio between variance and the square of the local radius. This analysis demonstrates clearly the conditions required for channel

expansion to yield decreases in solute variance. We also developed further simplifications of our model which yields a single, first-order nonlinear ODE describing relation between the axial radius distribution and variance (spatial) distribution. This relation is very useful in the design of channel shapes which yield specific (desired) dynamics for solute variance. We also evaluated a naive prediction of solute dynamics using the closed-form expression of the dispersion coefficient. The results showed this expression yields highly inaccurate estimates of the time evolution of variance, even in the simple cases of diverging and converging conical (section) channels.

We applied our model to several interesting test cases and benchmarked its performance relative to Brownian dynamics simulations. First, we demonstrated our model yields accurate predictions (relative to Brownian dynamics) of area-averaged solute dynamics in diverging and converging (conical) channels. Second, we applied our model to predict solute dynamics for various periodic channels, and again demonstrated excellent agreement with Brownian dynamics simulations. For the latter, we considered an initial condition and regime where channel expansions result in substantial decreases in variance (i.e. negative solute variance growth). We further analyzed the long-term (many period) development of solute in periodic channels by defining a long-term effective dispersion coefficient. We analyzed three separate periodic channel shapes and showed this long-term behavior is affected mostly by channel (axial) period and the magnitude of the fluctuation of the radius function. For the case of sinusoidal channels, our model demonstrated excellent comparison with a previously published model.

The third example application of our model was for an arbitrarily shaped channel. We here selected some complex channel shape which demonstrated strong advective dispersion effects. Again, our model showed excellent comparison with Brownian dynamics simulations, including capture of the positive and negative growth in variance when the solute zone experiences constriction or expansion in the channel.

Lastly, we demonstrated the power of our analytical approach by designing two channels that can control the spatial evolution of the solute so as to produce a desired spatial distribution of the solute variance. For the latter work, we first designed a channel that can maintain an approximately

constant solute variance. We then demonstrated a channel geometry which produces a sinusoidal axial distribution of variance as the solute develops in the channel.

Overall, our analysis provides a fairly accurate (according to Brownian dynamics simulation), fast, and easy-to-use model for solute dynamics in axisymmetric channels of arbitrary variance.

5 Acknowledgements

R.C. gratefully acknowledges support from the Stanford University Bio-X SIGF Fellows Program and from the Ministry of Education in Taiwan.

6 Declaration of Interests

The authors report no conflict of interest.

References

- (1) Brenner, H.; Edwards, D. A. *Macrotransport Processes*; 1993; pp 3–28.
- (2) Taylor, G. I. Dispersion of soluble matter in solvent flowing slowly through a tube. *Proceedings of the Royal Society of London. Series A. Mathematical and Physical Sciences* **1953**, *219*, 186–203.
- (3) Aris, R. On the dispersion of a solute in a fluid flowing through a tube. *Proceedings of the Royal Society of London. Series A. Mathematical and Physical Sciences* **1956**, *235*, 67–77.
- (4) Bryden, M. D.; Brenne, R. H. Multiple-timescale analysis of Taylor dispersion in converging and diverging flows. *Journal of Fluid Mechanics* **1996**, *311*, 343–359.
- (5) Hoagland, D. A.; Prud'Homme, R. K. Taylor-ariss dispersion arising from flow in a sinusoidal tube. *AIChE Journal* **1985**, *31*, 236–244.

- (6) Adrover, A.; Venditti, C.; Giona, M. Laminar dispersion at low and high Peclet numbers in a sinusoidal microtube: Point-size versus finite-size particles. *Physics of Fluids* **2019**, *31*, 062003.
- (7) Langlois, W. E.; Deville, M. O. *Slow viscous flow*; Springer, 1964; Vol. 173436.
- (8) Dispersion in flows with streamwise variations of mean velocity: Radial flow. *Industrial and Engineering Chemistry Research* **1999**, *38*, 851–854.

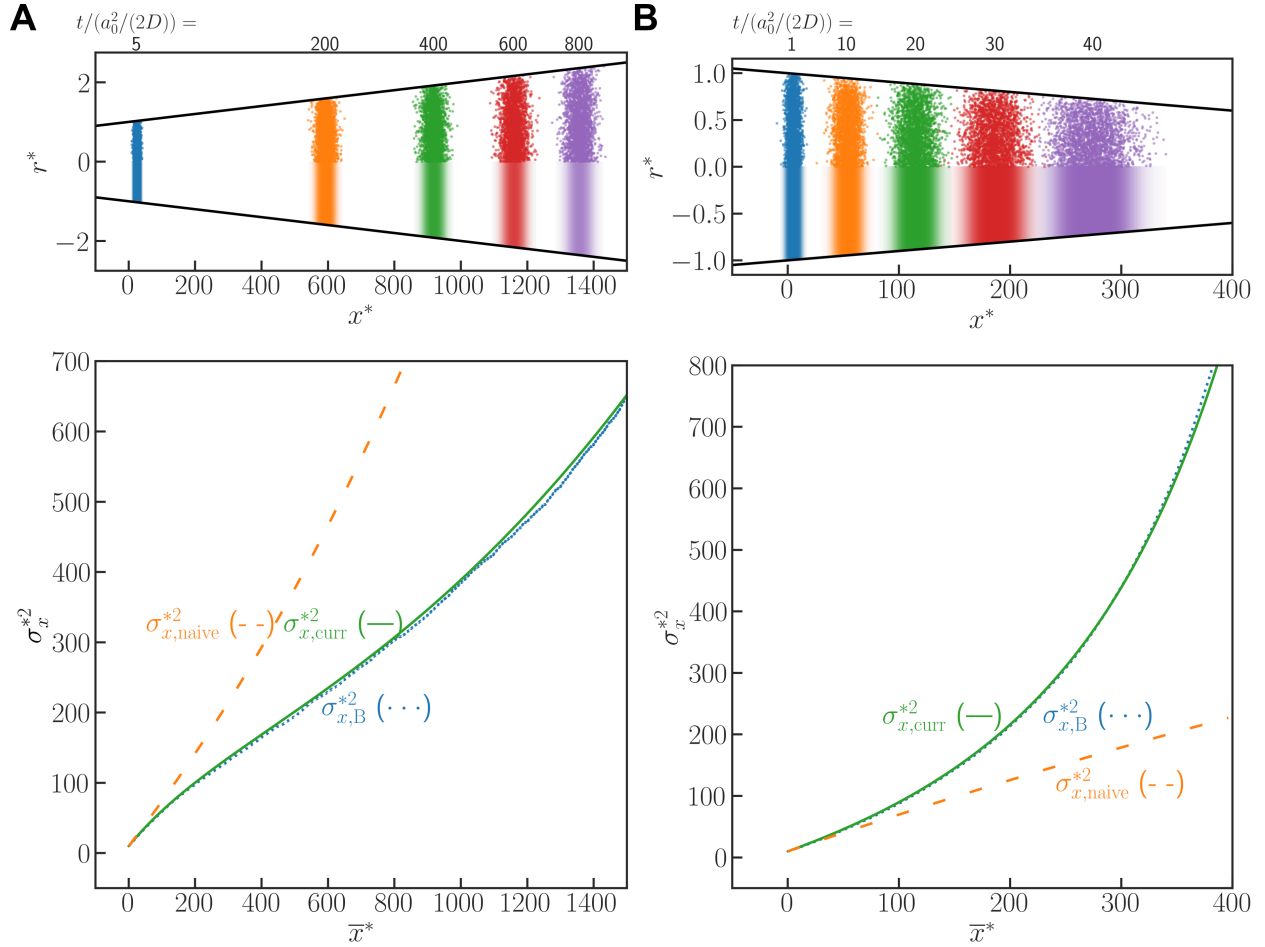


Figure 3: Taylor-Aris dispersion in (A) diverging and (B) converging conical channels. The plots in the top row show results from Brownian dynamic simulation (upper half) along with the predicted axial distribution of area-averaged concentration (bottom half). The bottom two plots show solute variance as a function of \bar{x}^* . Plotted are variance from the current analytical model (subscript "curr", closed-form Equation 16) and from Brownian dynamics simulation (subscript "B"). Also shown for reference is a naive prediction resulting from a simple time integration of variance based on Equation 19. Variance computed using Equation 16 shows excellent agreement with Brownian dynamics simulations. The naive method overestimated the growth of variance in the diverging channel while underestimating the growth of variance in the converging channel.

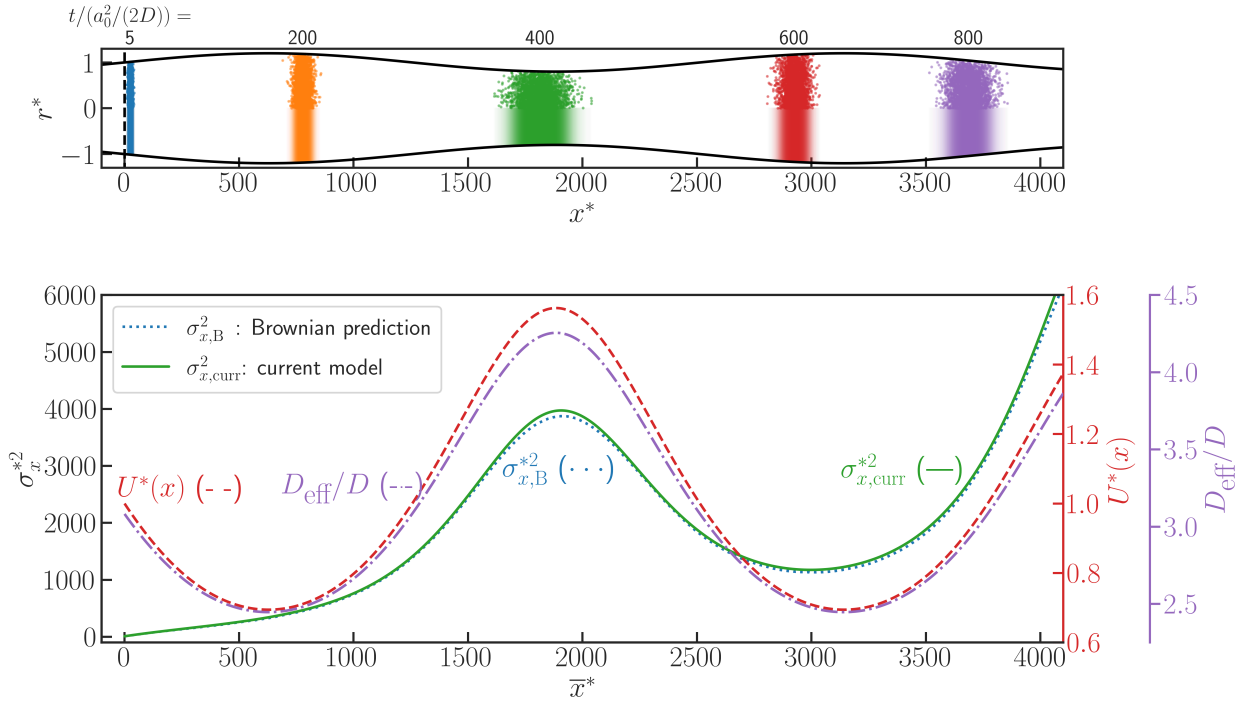


Figure 4: Taylor-Aris dispersion in a channel with a sinusoidal (periodic) radius distribution, $a(x)$. The top plot shows results from a Brownian dynamic simulation (upper half) and axial solute distribution predicted with the current model (closed form Equation 16). The bottom plot shows distribution of $\sigma_{x,B}^{*2}$, $\sigma_{x,curr}^{*2}$, $U^*(x)$, and D_{eff}/D , each as a function of the non-dimensional axial location along the channel, x/a_0 . $U^*(x)$ and D_{eff}^* are periodic functions and shown as a reference. Variance computed using Equation 16 shows excellent agreement with Brownian dynamics simulations. Note variance averaged along the axial spatial period increases monotonically as expected.

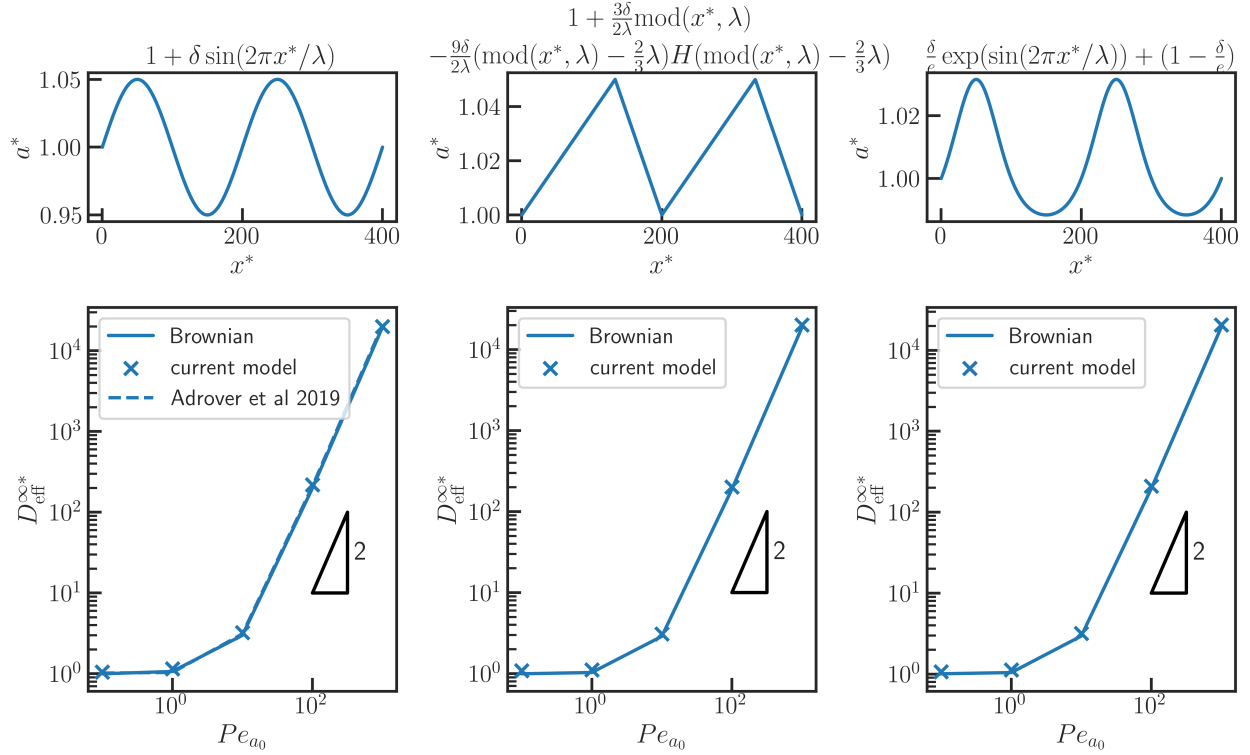


Figure 5: Normalized long-term effective dispersion coefficient $D_{\text{eff}}^{\infty*}$ as a function of Pe_a for three different periodic channels with equal period and similar radius amplitude ($\delta = 0.05$, $\lambda = 200$). All plots show the $D_{\text{eff}}^{\infty*}$ computed using Eq.16 and with a Brownian dynamics simulation. The plot on the left also shows a comparison with the closed-form expression derived by Adrover et al. (2019) for a sinusoidal channel.⁶ Note the plots across all three channels are very similar (but not exactly the same) in magnitude and shape. This similarity reflects that fact that the long-term development of the solute in periodic channels is most strongly a function of channel amplitude and a weak function of channel shape.

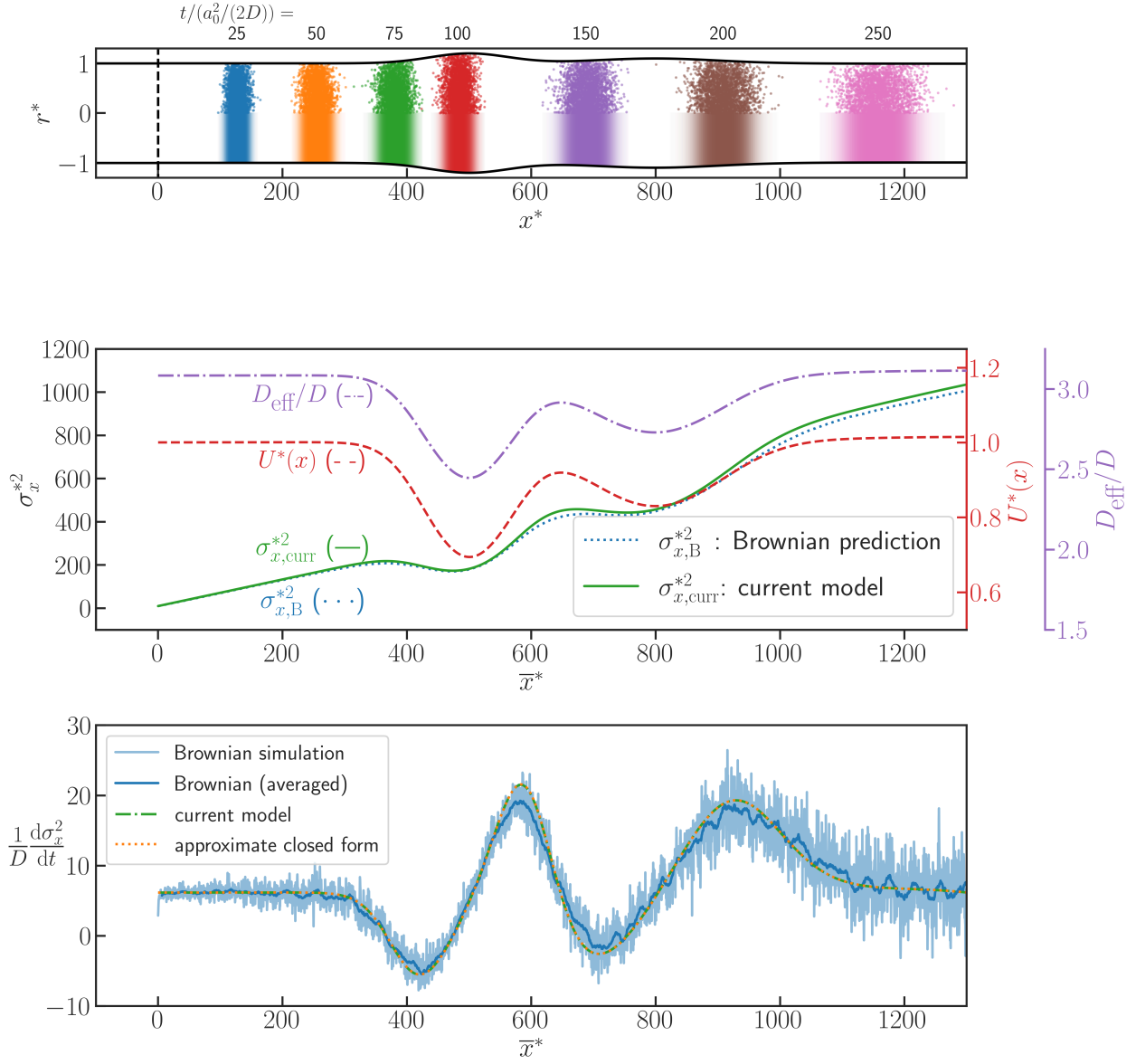


Figure 6: Taylor-Aris dispersion for an example arbitrarily shaped axisymmetric channel. The top plot shows results from a Brownian dynamic simulation (upper half) and axial solute distribution predicted with the current model (closed-form Equation 16). The middle plot shows distribution of $\sigma_{x,B}^{*2}$, $\sigma_{x,curr}^{*2}$, $U^*(x)$, and D_{eff}/D , each as a function of the non-dimensional axial location along the channel. $U^*(x)$ and D_{eff}/D are shown as a reference. Variance computed using Equation 16 shows excellent agreement with Brownian dynamics simulations. The bottom plot shows the same example used for demonstration and benchmarking of Equation 17. Plotted is a scaled rate of change of variance as a function of mean solute position \bar{x} as computed using Equation 16 and analytical expression Equation 17. Both of these solutions are compared to calculations based on a Brownian dynamics simulation. The blue curve is the Brownian smoothed with a moving average with a windows size of $\Delta t^* = 2.5$, while the light blue curve is the original Brownian simulation results.

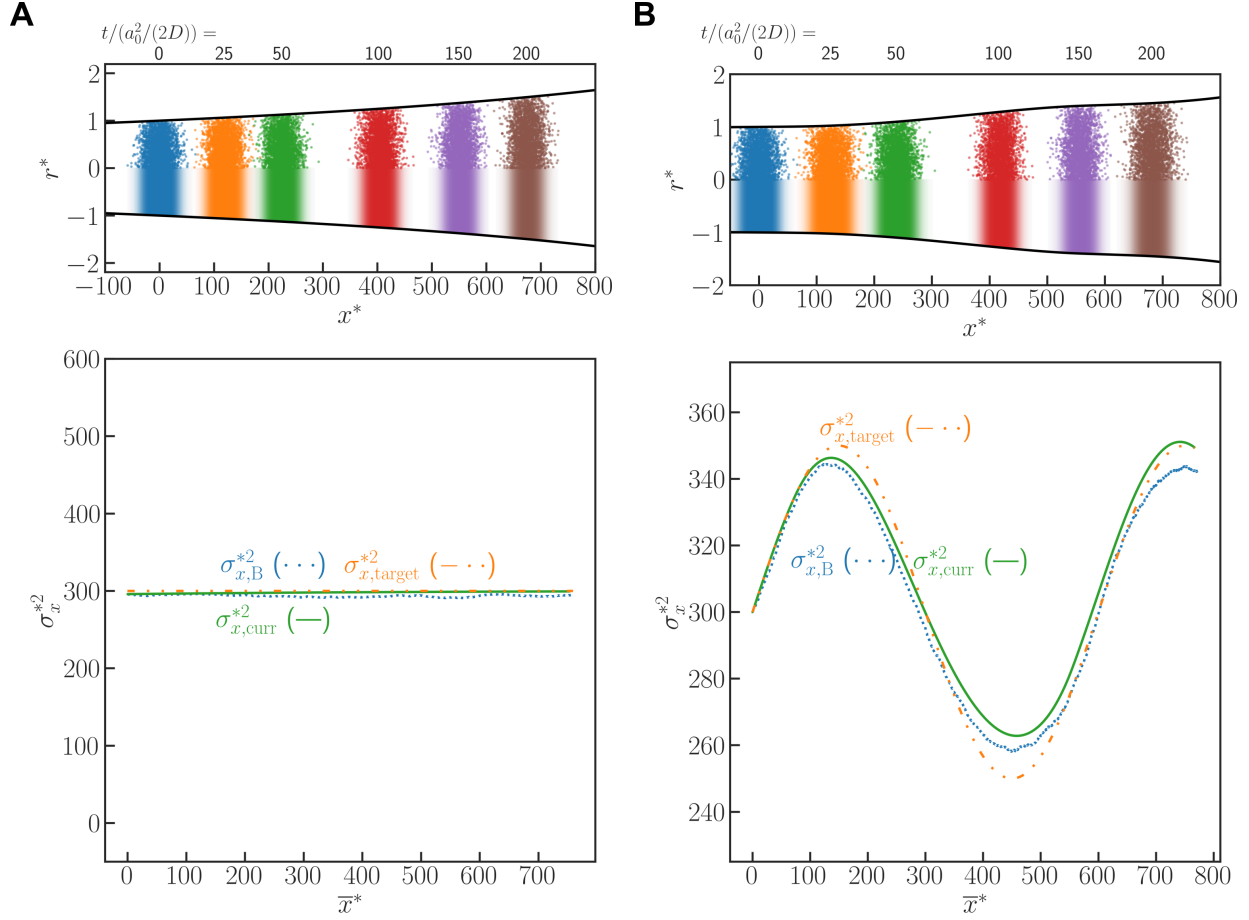


Figure 7: Engineering the variance evolution in Taylor-Aris dispersion. Using Equation 18, we designed two channels which (A) maintain an approximately constant variance and (B) result in a sinusoidal (axial) variation of variance as the solute develops in the channel. The top plot shows results from a Brownian dynamic simulation (upper half) and axial solute distribution predicted with the current model (closed form Equation 16). The bottom plot shows distribution of $\sigma_{x,B}^{*2}$, $\sigma_{x,curr}^{*2}$, and $\sigma_{x,target}^{*2}$, each as a function of the non-dimensional axial location along the channel. Variance computed using Equation 16 and variance computed from Brownian dynamic simulation both show excellent agreement with the targeted variance evolution pattern.

Taylor dispersion in arbitrarily shaped axisymmetric channels

Supplementary Information

Ray Chang[†] and Juan G. Santiago^{*,‡}

[†]*Department of Bioengineering, Stanford University, Stanford, CA, 94305, United States*

[‡]*Department of Mechanical Engineering, Stanford University, Stanford, CA, 94305, United States*

E-mail: juan.santiago@stanford.edu

Contents

A Comparison of effective dispersion coefficient in periodic channel with solution by Adrover et al.	3
B Supplementary figures	4

A Comparison of effective dispersion coefficient in periodic channel with solution by Adrover et al.

Adrover et al comprehensively analyzed effective diffusivity in a wide range of wavelength for a periodic channel with a specific radius $R(x) = R_0(1 + \delta \sin(2\pi x/(\lambda R_0)))$.[?] For our current model, the Taylor dispersion analysis requires that the flow field in the channel to be well approximated by lubrication theory. This constraint in turn requires the ratio (λ) of the channel wavelength to channel radius to be significantly greater than unity. In this limit, Adrover et al provided the following asymptotic formula for the effective dispersion coefficient in the sine-wave channel as

$$\begin{aligned}
 D_{\text{eff}}^{\infty*} &= D_0^* + \epsilon^2 D_1^* + \epsilon^4 D_2^* + \dots \\
 \lim_{\text{Pe}_\lambda \rightarrow \infty} D_0^* &= \frac{16 + 120\delta^2 + 90\delta^4 + 5\delta^6}{16(1 + \delta^2/2)} \\
 D_1^* &= \frac{\text{Pe}_\lambda^2 (1 + 3\delta^2 + 3\delta^4/8)}{48 (1 + \delta^2/2)^3} \\
 D_2^* &= \text{Pe}_\lambda^2 \frac{43\pi^2\delta^2(1 + 3\delta^2/2 + \delta^4/8)}{480(1 + \delta^2/2)^3}
 \end{aligned} \tag{S1}$$

Here, $\epsilon^2 = \lambda^{-2}$ and $\text{Pe}_\lambda = \lambda \frac{UR_0}{D}$ is the Peclet number defined based on wavelength.

B Supplementary figures

The top row of Figure S1 shows plots of the Brownian dynamics simulations for the simple diverging and converging channels shown in Figure 3 of the main paper. The bottom row here shows plots of the axial skewness and excess kurtosis of the Brownian dynamics point distribution.

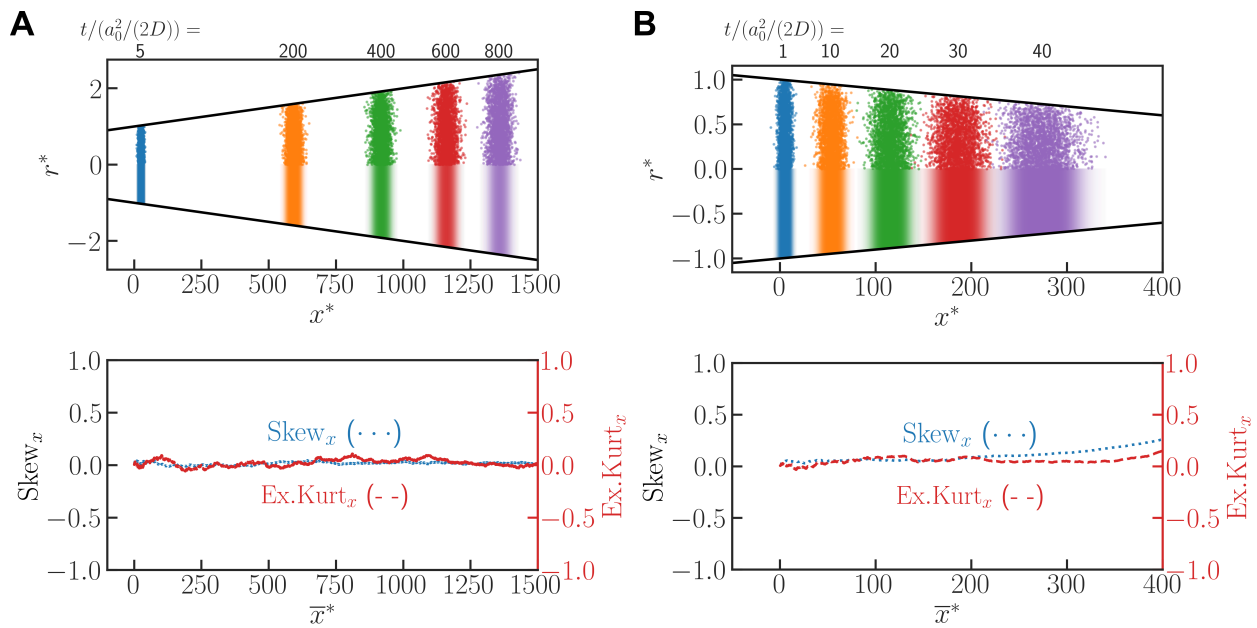


Figure S1: Taylor-Aris dispersion in (A) diverging and (B) converging conical channels. The plots in the top row show results from Brownian dynamic simulation (upper half) along with the predicted axial distribution of area-averaged concentration (bottom half). The bottom two plots show the axial skewness and excess kurtosis of solute zone (from Brownian simulation) as a function of \bar{x}^* . In both diverging and converging conical channels, the skewness and excess kurtosis of solute zone are negligible over the region analyzed. The results support our assumption of an approximately normal distribution for the area-averaged solute concentration along the axial direction (see Section 2.2 and 3.1 of the main manuscript).

Figure S2 shows plots of the Brownian dynamics simulations for the channel with a sinusoidal radius distribution (top) and plots of axial skewness and excess kurtosis of the Brownian dynamics point distributions (bottom). The top plots and conditions are the same to those of Figure 4 of the main paper.

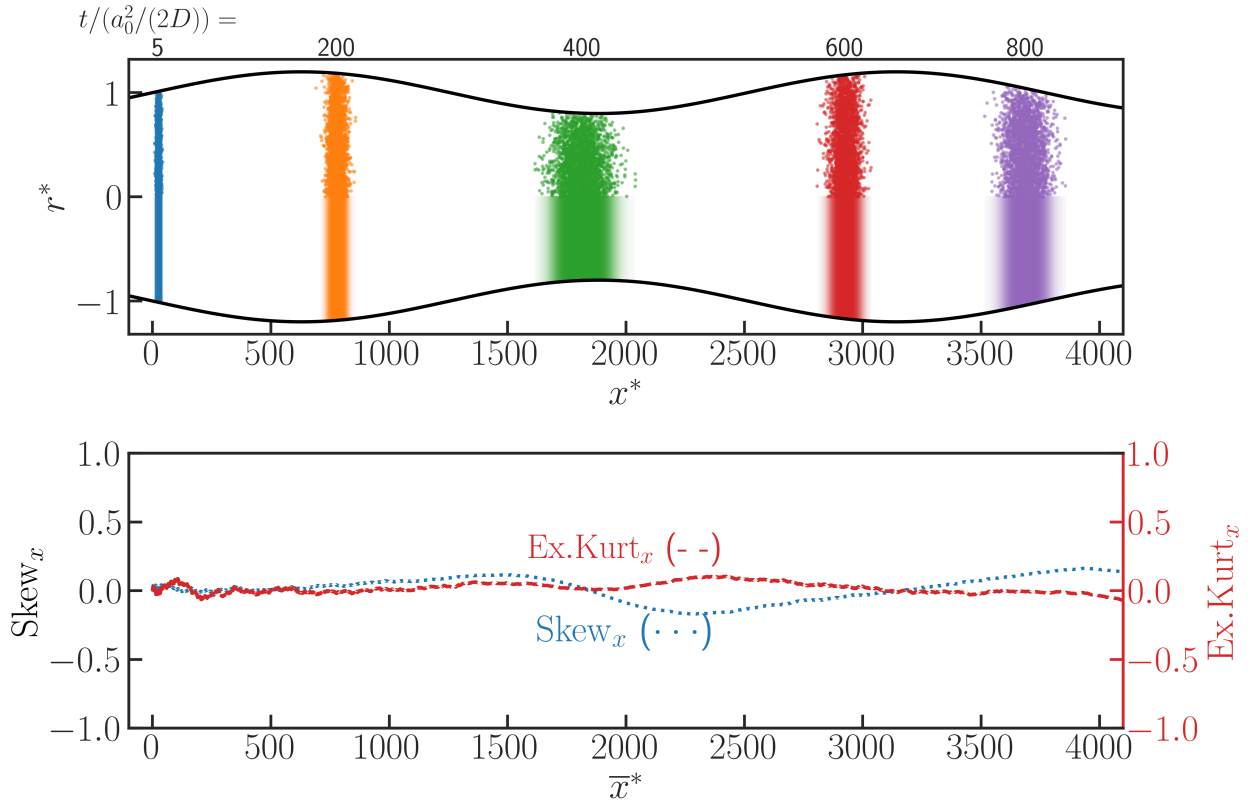


Figure S2: Taylor-Aris dispersion in a channel with a sinusoidal radius distribution, $a(x)$. The top plot shows results from Brownian dynamic simulation (upper half) along with the predicted axial distribution of area-averaged concentration (bottom half). The bottom plot shows the axial skewness and excess kurtosis of solute zone (from Brownian dynamics) as a function of \bar{x}^* . The skewness and excess kurtosis of solute zone are each negligible for the regions analyzed. The results support our assumption of normal distribution of area-averaged solute concentration along the axial direction (c.f. Section 2.2 and 3.2 of main paper).